Editors' Suggestion

UTe_2: A narrow-band superconductor

Martin Sundermann,[1,2,*] Takaki Okauchi,[3,*] Naoki Ito,[3] Denise S. Christovam,[1,†] Andrea Marino,[1] Daisuke Takegami,[1,‡] Andrei Gloskovskii,[2] Priscila F. S. Rosa,[4] Jan Kuneš,[5] Shin-ichi Fujimori,[6] Liu Hao Tjeng,[1] Andrea Severing,[1,7,§] and Atsushi Hariki[3,‖]

[1]*Max Planck Institute for Chemical Physics of Solids, Nöthnitzer Straße 40, 01187 Dresden, Germany*
[2]*PETRA III, Deutsches Elektronen-Synchrotron DESY, Notkestraße 85, 22607 Hamburg, Germany*
[3]*Department of Physics and Electronics, Osaka Metropolitan University, 1-1 Gakuen-cho, Nakaku, Sakai, Osaka 599-8531, Japan*
[4]*Los Alamos National Laboratory, Los Alamos, New Mexico 87545, USA*
[5]*Department of Condensed Matter Physics, Faculty of Science, Masaryk University, Kotlářská 2, 611 37 Brno, Czechia*
[6]*Materials Sciences Research Center, Japan Atomic Energy Agency, Sayo, Hyogo 679-5148, Japan*
[7]*Institute of Physics II, University of Cologne, Zülpicher Straße 77, 50937 Cologne, Germany*

(Received 28 August 2025; accepted 28 October 2025; published 20 November 2025)

We investigate the nature of the $5f$ electrons in the unconventional odd-parity superconductor UTe_2, focusing on the degree of covalency, localization versus itinerancy, and dominant electronic configuration. This is achieved using density functional theory (DFT) in combination with dynamical mean-field theory (DMFT) calculations. A key aspect of our approach is the material-specific tuning of the double-counting correction parameter, $\mu_{\rm dc}$, within the DFT + DMFT part. This tuning is guided by the energy dependence of photoionization cross sections in valence band photoelectron spectroscopy. The reliability of the parameters is confirmed by the accurate reproduction of the angle-resolved valence-band photoemission spectra and the U $4f$ core-level data. The DFT + DMFT model reveals that in UTe_2 U $5f^n$ configurations with $n = 1$–4 contribute to the ground state, with the $5f^2$ configuration being most prevalent and an average $5f$ shell filling close to 2.5. The model further suggests that the $5f$ electrons form narrow bands and that charge fluctuations due to degeneracy play a role in addition to coherent valence dynamics arising from hybridization with the conduction bath. Additionally, the significance of the U $6d$ states in UTe_2 is discussed.

DOI: 10.1103/t6hm-q647

I. INTRODUCTION

The heavy-fermion and spin-triplet superconductor UTe_2 [1–3] has generated significant interest due to the potential for the triplet pairing to induce nontrivial topological properties. UTe_2 crystallizes in the orthorhombic $Immm$ structure, exhibiting distinct anisotropies in transport properties and magnetization in the normal state. Superconductivity emerges below the critical temperature $T_c = 2.1$ K [4], with a highly anisotropic upper critical field that far exceeds the Pauli limit expected for even-parity superconductors [5,6].

The phase diagram of UTe_2 is highly tunable, exhibiting competing superconducting and (meta)magnetic phases. Two superconducting phases are observed as a function of applied b-axis field, with a metamagnetic transition to a field-polarized phase at even higher fields, which includes a field-induced superconducting pocket for fields applied 35° away from the b axis. Moderate hydrostatic pressure initially suppresses superconductivity but later another superconducting phase appears [5,7,8]. As pressure increases further, an antiferromagnetic phase emerges [9,10], followed by a phase transition from orthorhombic to tetragonal ($I4/mmm$) structure between around 5 and 7 GPa [10–14]. This transition is marked by a volume collapse of about 10% and a 4% increase of the uranium-uranium distance $d_{\rm UU}$. Notably, $d_{\rm UU}$ is above the Hill limit at all pressures. Applied pressure also affects the average orbital moment as well as the average $5f$ shell filling, $\langle n_f \rangle$, which initially decreases but recovers at the crystallographic phase transition [14,15].

In this work, we address the degree of covalence of the $5f$ electrons in UTe_2, as the hybridization of f electrons with the conduction electron bath plays a crucial role in the physics of actinide compounds. A key challenge in uranium compounds is the strong hybridization between the $5f$ and conduction electrons, due to the spatially extended nature of the $5f$ shell. Additionally, multiple electronic configurations contribute to the ground state, resulting in the average

*These authors contributed equally to this work.
†Present address: Max Planck Institute for Solid State Research, Heisenbergstraße 1, 70569 Stuttgart, Germany.
‡Present address: Department of Physics, Tokyo Metropolitan University, Hachioji, 192-0397, Japan.
§Contact author: andrea.severing@cpfs.mpg.de
‖Contact author: hariki@omu.ac.jp

uranium valence deviating strongly from integer values [16,17]. Consequently, determining the most relevant electronic configuration, typically $5f^2$ or $5f^3$, that defines the ground state's quantum numbers, as well as understanding the distribution of configurations contributing to the ground state, provides important insights and a route toward the long-sought microscopic model of actinide materials.

Unfortunately, in uranium compounds, this information remains elusive in commonly applied experiments. X-ray absorption (XAS) and core-level photoelectron spectroscopy (PES) data are broad and structureless and do not provide sufficient information for a quantitative analysis of the many-body ground state [18]. This challenge, along with the necessity of an Anderson-impurity-model (AIM)-based approach accounting for both the strong correlation of U $5f$ electrons and their hybridization, has resulted in conflicting interpretations of uranium spectroscopy data and ongoing discussions about the dominant local electronic configuration in the normal state [10,15,19–24].

Recently, some of us demonstrated how the dilemma regarding the ground-state configuration can be addressed using valence band resonant inelastic x-ray scattering (VB-RIXS). VB-RIXS offers unique insights into the dominant electronic configuration, particularly when performed at the U $M_{4,5}$ edges, where the signal-to-background ratio is excellent [25]. Applying this technique to UTe_2, multiplet excitations characteristic of the $5f^2$ configuration [26] were observed. The detection of these excitations, along with successful modeling using ionic calculations, suggests that the $5f$ electrons in UTe_2 are strongly correlated [24,26]. Additionally, the observation of charge transfer scattering in M-edge VB-RIXS spectra provides further evidence of the strongly noninteger valent nature of UTe_2.

This raises the question of the *degree* of correlation or itinerancy in the noninteger valent ground state of UTe_2. In principle, PES is sensitive to covalency [27–30], but intrinsic broadening also limits the information of U core-level PES spectra; they exhibit a single broad emission line and at most one satellite feature (see, e.g., Refs. [21,31,32]).

In Ref. [33], we demonstrated that interpreting U $4f$ core-level data for uranium intermetallic compounds are not straightforward. Using two isostructural model compounds, Pauli paramagnetic UB_2 and ferromagnetic UGa_2 ($T_C = 125\,\mathrm{K}$, $\mu_{\mathrm{ord}} = 3\,\mu_B$), which represent the more extreme ends of the delocalization spectrum, we showed that density functional theory (DFT) combined with dynamical mean-field theory (DMFT) with material-specific parameters is essential to account for correlation effects and to gain insight into the degree of delocalization. Key computational parameters, including the double-counting correction μ_{dc}, the Hubbard U_{ff}, and Hund's J of the U $5f$ states, were optimized to accurately reproduce the valence band (VB) spectra measured with PES using both hard and soft x-rays. The use of two very different x-ray energies allows for clear distinction between the correlated $5f$ and the other, weakly correlated, orbitals near the Fermi energy, due to the different energy dependence of their respective photoionization cross sections [34–36]: In the soft x-ray regimes, the signal from the $5f$ states dominates, while at 6000 eV, the non-$5f$ states are strongly enhanced.

In this study, we extend this approach to UTe_2, utilizing DFT + DMFT calculations with parameters tuned to reproduce experimental VB PES spectra at both 6000 and 800 eV, angle-resolved PES (ARPES) at 565–675 eV as well as core-level PES. Once the electronic model is established by setting the parameters (μ_{dc}, U_{ff}, and J) in the model Hamiltonian, the respective weights of $5f$ configurations in the intermediate valent ground state are determined and the time-dependent charge correlation function is calculated.

II. METHODS

A. Experiment

The VB PES and ARPES data, measured at beamline BL23SU at SPring-8 [37] at 20 K with 800 and 556–675 eV incident energy, respectively, and energy resolutions of 140 and 100 meV, are adapted from Ref. [19]. The hard x-ray VB PES data with 6000 eV incident energy and resolution of 230 meV are adapted from Ref. [26]. The core-level PES measurements with hard x-rays (HAXPES) were performed on the same set of platelike single crystalline samples of UTe_2 as in Ref. [26] and measured under the same conditions, i.e., at P22 beamline [38] at PETRA III (DESY) in Hamburg, Germany, with 6000 eV incident energy, an overall resolution of ≈230 meV, and temperature $T = 40\,\mathrm{K}$.

B. Calculations

The computational modeling of UTe_2 followed the same philosophy as in Ref. [33]. We began by performing a standard DFT calculation for the experimental crystal structure [39], using the local density approximation (LDA) for the exchange-correlation functional and incorporating spin-orbit coupling, as implemented in the WIEN2K package [40]. Based on the resulting DFT band structure, we constructed a tight-binding model including U $5f$, $7s$, $6d$, $7p$ and Te $5s$, $5p$ orbitals [41,42]. The lattice model was then augmented with local Coulomb interactions among the U $5f$ electrons, parameterized by the Hubbard U_{ff} and Hund's J, and solved using DMFT [43,44]. The self-energy of the U $5f$ electrons was computed from the AIM using the continuous-time quantum Monte Carlo method [45–48], retaining only the density-density terms of the Coulomb vertex for computational efficiency. Upon convergence of the DMFT self-consistency loop, the VB spectrum was obtained by analytic continuation of the self-energy using the maximum entropy method [49]. All calculations were performed at $T = 300\,\mathrm{K}$.

In the DFT + DMFT modeling, determining the double-counting correction μ_{dc} is a crucial step to account for the f-f interaction effects already present at the DFT level [44,50,51]. The U $5f$ orbital energies in the DMFT model are obtained by shifting their corresponding DFT values by μ_{dc}; hence, the choice of μ_{dc} is essential for correctly representing the uranium valency. Although no universally accepted expression for μ_{dc} exists, it effectively renormalizes the energy separations between the correlated U $5f$ states and the uncorrelated bands. A realistic value of μ_{dc} can therefore be determined by tuning it to reproduce the experimental VB PES spectrum [33], measured at very different photon energies as described

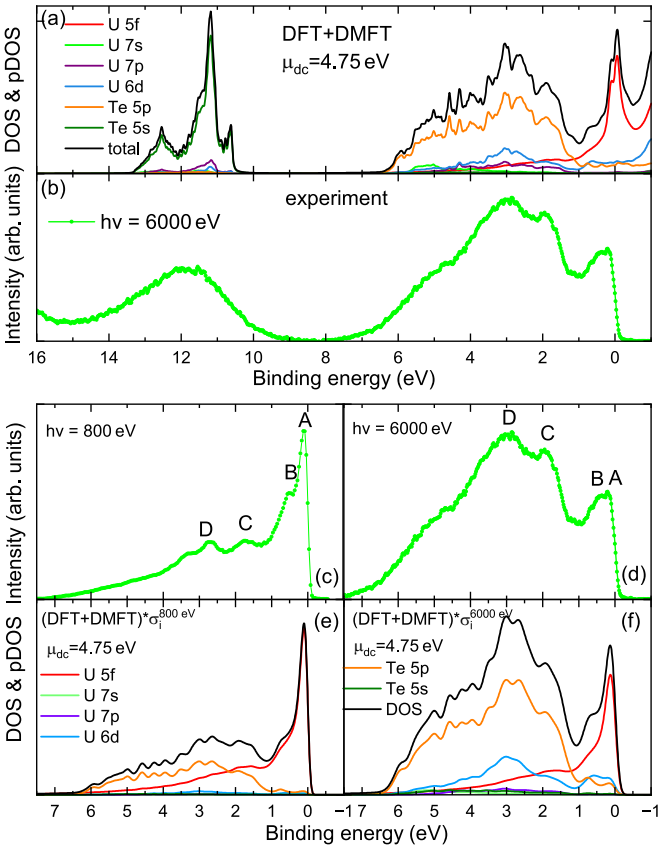

FIG. 1. (a) Valence band spectra: total DOS (black) and orbital-resolved DOS (color) from the DFT + DMFT calculations with $U_{\rm ff} = 3\,$eV, $J = 0.59\,$eV, and optimized $\mu_{\rm dc} = 4.75\,$eV. (b) Hard x-ray VB PES data adapted from Ref. [26]. (c), (d) VB PES data over a smaller energy range, measured with soft [19] and hard x-rays, respectively. The labels *A*, *B*, *C*, and *D* indicate characteristic spectral features. (e), (f) Total and orbital-resolved DOS from the same DFT + DMFT calculations as in panel (a), multiplied by the Fermi function and respective photoemission cross sections, and broadened to account for experimental resolution.

above. To further validate the optimized DMFT model, both ARPES and core-level spectra are calculated and compared to experimental data; the ARPES comparison confirms the model's accuracy with respect to the low-energy bands, while the core-level comparison, it being sensitive to covalency and f-configuration energies [33], offers complementary support for the electronic model. The computational details for these spectra follow the methodology of Refs. [33,52].

III. RESULTS AND DISCUSSION

A. DFT + DMFT modeling of UTe_2

Figure 1(a) shows the spectral functions for UTe_2 as obtained from our DFT + DMFT calculations for $U_{\rm ff} = 3\,$eV, $J = 0.59\,$eV, and the optimized value for $\mu_{\rm dc} = 4.75\,$eV in the energy window -1 to 16 eV. The comparison to experimental VB data in panel (b), here measured with hard x-rays, confirms that the main features are well captured, that is, the peak close to the Fermi energy, a broad humplike signal between 1 and 6 eV, and the signal close to 12 eV. The last one is due to Te 5*s* states.

For further identification of subshells, especially close to the Fermi energy, we inspect the energy dependence of spectral features in a smaller energy range. In Figs. 1(c) and 1(d), we compare the VB data of UTe_2 measured with 800 and 6000 eV incident energy. We observe a strong change in spectral shape, which is due to the different energy dependence of the subshells' cross sections. Most strikingly, the soft x-ray data peak sharply close to the Fermi energy (see peak labeled *A*), followed by a shoulder (*B*), and some smaller spectral weight with some structure, labeled with *C* and *D*. Spectral weight *A* is strongly suppressed in the hard x-ray spectra in panel (d). Only a broader hump consisting of *A* and *B* survives, while the broad spectral weight with features *C* and *D* around 2 and 3 eV binding energies, respectively, is strongly enhanced. The $5f$ signal being ten times stronger than the non-$5f$ in the 800 eV data, let us safely conclude that the feature closest to the Fermi energy must be mainly due to the $5f$ states. In contrast, features *C* and *D* must consist mainly of non-$5f$ states.

Figures 1(e) and 1(f) show the same DFT + DMFT VB spectra as in panel (a), now multiplied with the Fermi function and broadened to account for resolution effects, and corrected for the respective cross sections for 800 and 6000 eV (see Table I, Appendix A). A comparison between the experimental data in panels (c) and (d) and total calculated density of states (DOS) (black lines) in panels (e) and (f) demonstrates that the intensity variations of spectral weights close to the Fermi energy, as well as the broad distribution around 3 eV with varying incident energy, are best reproduced for the present choice of parameters. In Appendix C, Fig. 6(a), we show the sensitivity of the calculated VB spectra to $\mu_{\rm dc}$.

Upon close inspection of Figs. 1(c)–1(f), we find that the intensities *A* and *B* near the Fermi energy are predominantly due to the U $5f$ states (red lines), but not purely. Also, Te $5p$ (orange) and U $6d$ (blue) states have some spectral weight below 1 eV binding energy. Meanwhile, the spectral features *C* and *D* are primarily composed of Te $5p$ states, with some contribution from the U $5f$ and U $6d$ states.

To further validate our choice of parameters, experimental ARPES spectra are compared with the optimized DFT + DMFT results along selected momentum paths (see Fig. 2). We find good agreement between experiment and theory when keeping in mind that the soft x-ray experiment enhances the $5f$ states with respect to the other states, something not accounted for in the momentum-resolved spectral functions of Fig 2: The flat branch close to the Fermi energy and also the strongly dispersive band along the Γ–Z–X_1 path down to 1 eV are reproduced. The orbital-resolved spectral contributions from U $5f$, U $6d$, and Te $5p$ states, shown in Figs. 2(c)–2(e), reveal that the strongly dispersive band has dominant U $6d$ and Te $5p$ character. In addition, the narrow band near the Fermi level, as well as the enhanced spectral weight around 0.3–0.5 eV near the X_1 point, is due to $5f$ states. This agreement deteriorates rapidly when the double-counting parameter, i.e., the position of the U $5f$ level, is shifted away from its optimal value (see Appendix C, Fig. 7).

The model derived above also reproduces the U $4f$ core-level spectrum of UTe_2, as shown in Fig. 3 (see green dots), alongside the spectra of the two model compounds from Ref. [33] (see gray dots). The present hard x-ray data of

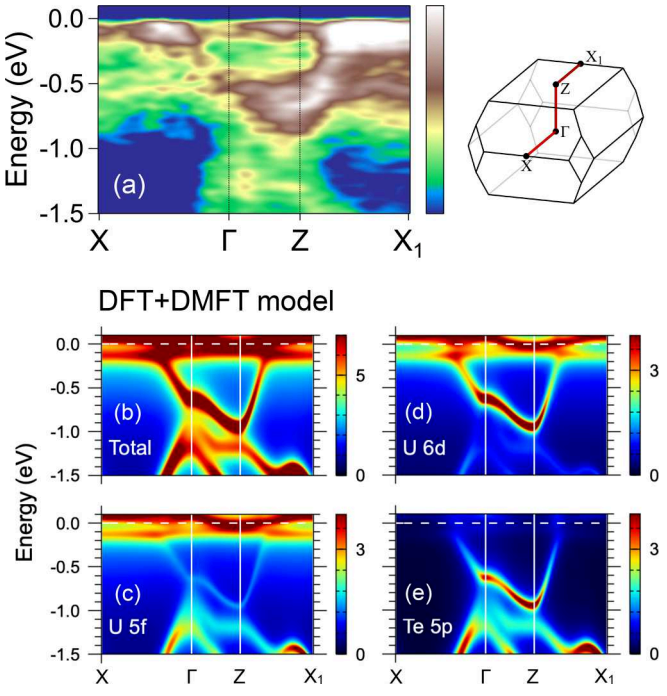

FIG. 2. (a) Experimental soft x-ray (800 eV) ARPES data of UTe_2 along the momentum path shown in the right panel. (Bottom) momentum-resolved spectral densities calculated from the optimized DFT + DMFT model. Panel (b) displays the total spectral densities, while panels (c), (d), and (e) show the orbital contributions from U $5f$, U $6d$, and Te $5p$ states, respectively.

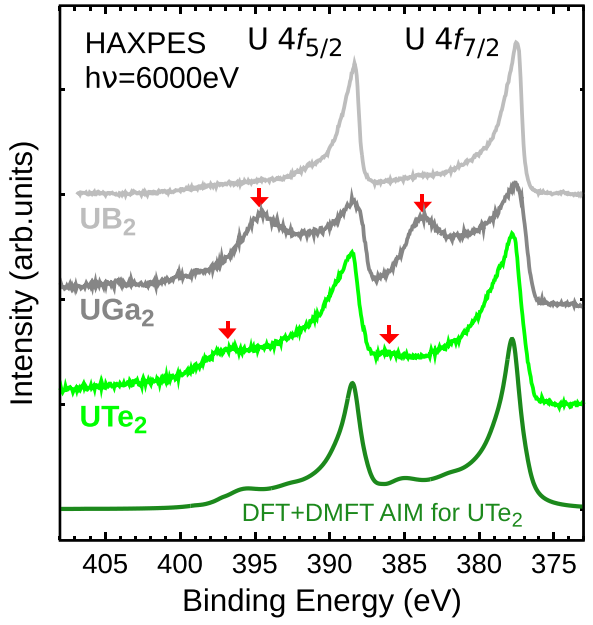

FIG. 3. U $4f$ core-level spectra of UTe_2 (light green), corrected for integrated background and plasmon contributions (see Appendix B), compared to those of UGa_2 (dark gray) and UB_2 (light gray), adapted from Ref. [33]. The dark green curve shows the calculated core-level spectra of UTe_2 using the DFT + DMFT AIM.

UTe_2 are consistent with previous soft x-ray results reported in Refs. [21,32,53]. The core-level spectra in Fig. 3 exhibit strong material dependence, with both the spectral weight and energy position of the satellite relative to the main line varying significantly (see red arrows). We calculated the core-level spectrum using the optimized DMFT model, incorporating the core-valeance interaction U_{fc} in the DFT + DMFT impurity framework. Good agreement with experiment is obtained for $U_{fc} = 5.0\,\text{eV}$ (see dark green line), a value consistent with those used for UGa_2 and UB_2 [33]. In Appendix C, Fig. 8, we show the sensitivity of the core-level line shape to μ_{dc} and U_{fc}, respectively, confirming that agreement with experiment is achieved only near this optimal μ_{dc} value.

B. U $5f$ occupation and charge correlation function

Having established the electronic model that reproduces the VB, ARPES, and core-level spectra, we now use this model to examine the degree of correlation and covalency in UTe_2. In Fig. 4, we start with the U valence histogram, computed from the DFT + DMFT results using the optimized model parameters, and compare it to the respective histograms of the model compounds UGa_2 and UB_2 from Ref. [33]. Additionally, we overlay the binomial distributions corresponding to the fully itinerant, noninteracting bandlike limit for the average filling given by DFT + DMFT [54]. For completeness, the variation of the $5f^n$ spectral weights with μ_{dc} is shown in Appendix C, Fig. 6(b).

In Ref. [33], we showed that UGa_2 is a strongly correlated compound dominated by the $5f^2$ configuration, while UB_2 represents a strongly itinerant system, close to the bandlike limit. Here, the width of the distribution of $5f^n$ configurations in the histogram serves as a measure of the magnitude of charge fluctuations between the relevant $5f$ configurations.

In UTe_2, we also find that the $5f^2$ configuration is the most prominent, consistent with the $5f^2$ multiplet structure observed in the VB-RIXS spectra [24,26]. Moreover, the distribution of $5f^n$ configurations deviates significantly from a binomial distribution and is considerably narrower than that of UB_2, reinforcing the characterization of UTe_2 as a strongly correlated material. However, the distribution in UTe_2 is slightly wider than that of UGa_2, indicating that the degree of charge dynamics in UTe_2 differs from that of the prototypically correlated uranium compound UGa_2. In fact, the histogram in UTe_2 is mainly composed of the configurations $5f^2$ and $5f^3$, with the center of gravity shifted toward higher occupations compared to UGa_2 and UB_2, resulting in an average $5f$ shell occupancy of $\langle n_f \rangle = 2.5$.

Further insight into the differences of the three compounds can be gained by examining the time dependence of the local charge correlation function $\langle \delta n(\tau)\delta n(0)\rangle$ in the DFT + DMFT results. In Fig. 4(d), we plot the logarithm of this function in the imaginary time domain for UTe_2 (green line) and, for comparison, also for UGa_2 and UB_2 [33] (black and gray lines).

The instantaneous value at $\tau = 0$ reflects the magnitude of charge fluctuations. UTe_2 exhibits stronger charge fluctuations than UGa_2, but weaker than UB_2, consistent with the respective width of the valence histograms in Figs. 4(a)–4(c). At finite τ, the charge correlation function of UTe_2 decays

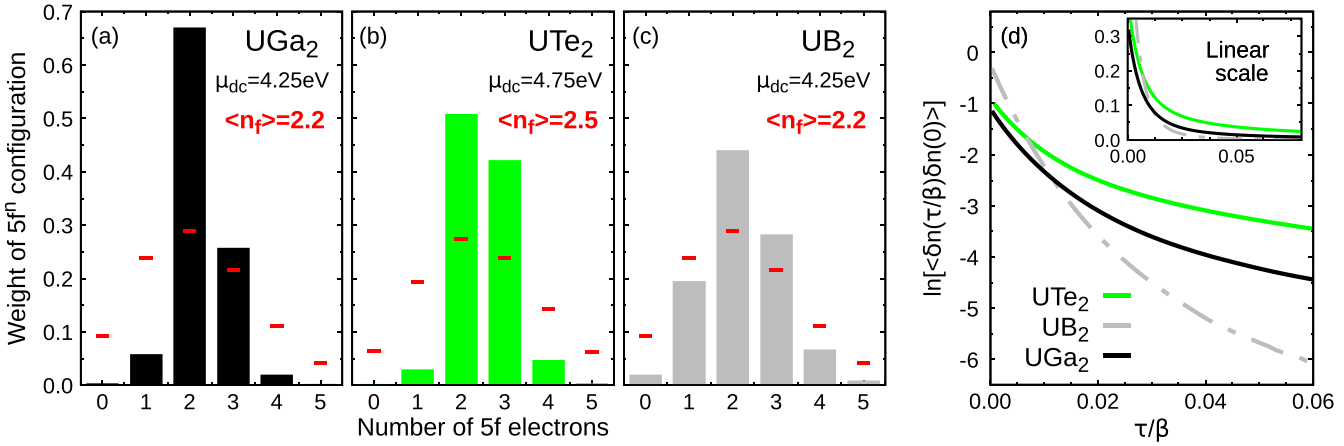

FIG. 4. (a)–(c) Valence histograms from DFT + DMFT of UGa_2, UTe_2 and UB_2, respectively, and binomial distribution (red ticks). (d) Logarithm of charge correlation function $\langle \delta n(\tau)\delta n(0)\rangle$ from DFT + DMFT for UTe_2 (green) and the two model compounds UGa_2 (black) and UB_2 (light gray). The data of UGa_2 and UB_2 are adapted from Ref. [33]. A linear-scale plot is shown in the inset.

more slowly than that of UGa_2, and exhibits a more pronounced constant component. Charge fluctuations between configurations may arise from two distinct mechanisms: (1) Covalency and itinerancy lead to a coherent admixture of valence states and are referred to as *intermediate valency*. It results in a rapid decay of $\langle \delta n(\tau)\delta n(0)\rangle$, as clearly observed in UB_2 and, to a lesser extent, in UGa_2. (2) Quasidegenerate configurations, e.g., $5f^2$ and $5f^3$, which give rise to long-lived, local fluctuations between valence states, are referred to as *mixed valency* [55]. In the extreme case of fully degenerate configurations without intersite coherence, this would produce a constant value of $\langle \delta n(\tau)\delta n(0)\rangle$ at finite τ. In UTe_2, the value at $\tau = 0$ indicates stronger charge fluctuations than in UGa_2, while the slower decay at finite τ reflects a different balance between the two charge-fluctuation mechanisms in these two materials. In UTe_2, the charge fluctuations stem to a larger extent from the degeneracy of $5f$ configurations, that is, from a smaller energy separation between the $5f^2$ and $5f^3$ states. However, because $\langle \delta n(\tau)\delta n(0)\rangle$ does not remain strictly constant over time, hybridization with the surrounding electron bath is still present, albeit to a lesser extend than in UGa_2. This makes UTe_2 a narrower-band material compared to UGa_2, consistent with the high tunability of its phase diagram [5–15].

The analysis of the charge correlation function provides insights into the satellites observed in the core-level spectra (see Fig. 3). The intensity and energy of these satellites are determined by a delicate balance among covalency, electron correlation, and configuration mixing. This analysis suggests that the satellites originate from distinct physical mechanisms: The weak satellite in UB_2 is a consequence of strong covalency and the strong satellite in UGa_2 is due to strong correlations and localization, while in UTe_2 it emerges from a subtle balance between f^2 and f^3 mixed valency.

C. Choice of model parameters in DFT + DMFT

Several DFT + DMFT studies have been performed on UTe_2, each adopting different choices of $U_{\rm ff}$ and J parameters, and different treatments of $\mu_{\rm dc}$, leading to variations in the U $5f$ spectral features near the Fermi level. Most of these studies estimate the U $5f$ occupation close to 2, in contrast to our estimate of 2.5. For example, Refs. [20,56] adopt a large $U_{\rm ff} = 6$–8 eV together with the so-called nominal double-counting scheme for $\mu_{\rm dc}$. To our knowledge, applying the nominal $\mu_{\rm dc}$ scheme, which assumes an electron count f^2 (or f^3) when evaluating the correction parameter $\mu_{\rm dc}$, to a mixed-valent f-electron system such as UTe_2 has not been validated against experimental data. In Ref. [57], the $U_{\rm ff}$ value is adjusted to reproduce a specific feature in the ARPES data, but neither the $\mu_{\rm dc}$ value nor the resulting U $5f$ occupation is provided. Reference [58], on the other hand, uses a different implementation of DMFT than the other works and reports a $5f$ occupation of 2.3.

In the following, we elaborate on our choice of model parameters for UTe_2 within the DFT + DMFT framework. To assess parameter sensitivity, we performed additional calculations using slightly different sets of $U_{\rm ff}$ and J, varying J between 0.47 and 0.7 eV for a fixed $U_{\rm ff} = 2.8$ eV, with corresponding adjustments to $\mu_{\rm dc}$. While different combinations of $U_{\rm ff}$ and J yield variations in both spectral shape and U $5f$ occupation, we find that the VB spectra converge to a similar shape that reasonably reproduces the experimental VB-PES data, provided that $\mu_{\rm dc}$ is individually tuned (Appendix C, Fig. 9). Minor differences in spectral peak positions or intensity ratios remain, as also discussed in Ref. [33]. Crucially, such agreement with experiment is achieved only when $\mu_{\rm dc}$ is adjusted such that the distribution of the $5f^n$ configurations in the ground state and average $5f$ occupation $\langle n_{\rm f}\rangle$ remains about the same, regardless of the specific values of $U_{\rm ff}$ and J within the studied range.

This underscores the critical role of accurately determining $\mu_{\rm dc}$ for predicting the correct uranium valency. As shown in Fig. 6(b) of Appendix C, even small variations in $\mu_{\rm dc}$ can significantly affect the calculated $5f$ occupation. While certain low-energy band features may be captured by adjusting $U_{\rm ff}$ or J alone, such adjustments lead to either over- or underestimation of the $5f$ occupation. This discrepancy in electron count immediately manifests in core-level PES, which is highly sensitive to the uranium valency, as demonstrated in Fig. 8. Therefore, the direct comparison with the comprehensive set of spectroscopic data presented here provides a valuable benchmark for evaluating the reliability of the

chosen parameters and the underlying electronic structure of UTe_2 with its nearly degenerate U $5f^2$ and $5f^3$ configurations and narrow $5f$ bands.

D. Importance of U 6*d* states

Our optimized DFT + DMFT model raises the question of how such a complex mixed-valence state is accommodated in the crystal structure of UTe_2. As pointed out in Ref. [26], one of the two Te sites cannot spatially accommodate a large Te^{2-} ion, which lead to the proposal of a hypothetical U^{3+} valence state, typically associated with a formal U $5f^3$ configuration. However, both the valence histogram obtained in this study and the previously reported RIXS data indicate the relevance of the $5f^2$ configuration. To reconcile this, Miao *et al.* [20] and Christovam *et al.* [26] suggested that the U 6*d* orbitals, particularly the $6d_{z^2-r^2}$ states, must absorb some of the charge.

To test this conjecture, we performed DFT + DMFT calculations with a modified model in which electron transfer between U $5f$ and U 6*d* states was effectively suppressed. This was achieved by shifting the onsite energies of the U 6*d* states by 3 eV, eliminating the U 6*d* states from the top of the VB. In Fig. 10 of Appendix D, we compare the original (a) and modified (b) DFT spectra. Although the U 6*d* weight near the top of the VB is not substantial in the original DFT model, it has a sizable impact on the U $5f$ valence state when correlations are taken into account. In the DFT + DMFT results for the modified model, a significant increase of the $5f$ occupation is observed. The $5f^3$ configuration becomes the most abundant over a broad range of the μ_{dc} values [see Appendix D, Fig. 11(b)]. This confirms the above conjecture that U 6*d* states provide the reservoir, which fixes the $5f$ occupation.

IV. SUMMARY

We investigated the degree of covalency, the nature of valence fluctuations, and the dominant $5f$ electronic configuration in UTe_2. To this end, DFT + DMFT calculations, using material-specific parameters derived from both hard and soft x-ray valence-band photoelectron spectroscopy data, were presented. Our DFT + DMFT model simultaneously reproduces the valence-band spectra, ARPES data, and U $4f$ core-level spectra, validating the chosen parameters. Our analysis underscores the importance of anchoring the choice of computational parameters, especially the double-counting correction μ_{dc} within the DFT + DMFT scheme, to experimental photoemission spectra in order to obtain reliable estimates of the $5f$ shell occupancy.

Our results yield an average $5f$ electron count of 2.5, with the $5f^2$ configuration being the most dominant and defining the quantum numbers of the ground state. UTe_2 is identified as a narrow-band material in which itinerancy still plays a role. We argue that the higher degree of localization in UTe_2, compared to the ferromagnet UGa_2, arises from the presence of quasidegenerate U $5f^2$ and $5f^3$ configurations, pointing to mixed valence rather than intermediate-valence behavior.

Finally, DFT + DMFT calculations on a modified model without U 6*d* states at the valence band show increased $5f$ shell filling, supporting the view that the U ion tends toward a 3+ valence. This suggests that, under realistic conditions, part of the charge is carried by the 6*d* states, as previously suggested in Ref. [26]. The artificial removal of the U 6*d* states, combined with correlation effects, significantly alters the low-energy valence-band structure, underscoring the importance of including U 6*d* states in modeling UTe_2.

TABLE I. Photoionization cross sections in kbarn (10^{-25}-m^2) at 800 and 6000 eV used to scale the Te and U valence states.

State	800 eV	6000 eV
U $5f$	23.7	0.075
U 6*d*	1.75	0.070
U 7*s*	0.84	0.025
U 7*p*	0.84	0.025
Te 5*p*	5.08	0.066
Te 5*s*	7.49	0.143

ACKNOWLEDGMENTS

A.H. was supported by JSPS KAKENHI Grants No. 25K00961, No. 25K07211, No. 23H03816, No. 23H03817, and No. 23K03324, and the 2025 Osaka Metropolitan University (OMU) Strategic Research Promotion Project (Young Researcher). S.-I.F. was funded by JSPS KAKENHI Grants No. 18K03553, No. 20KK0061, and No. 22H03874. Parts of the computations were performed at It4innovations funded by the Ministry of Education, Youth and Sports of the Czech Republic through the e-INFRA CZ (ID: 90254). A.S. acknowledges support from the German Research Foundation (DFG)—Grant No. 387555779. All authors acknowledge DESY (Hamburg, Germany), a member of the Helmholtz Association HGF, for the provision of experimental facilities. The soft x-ray experiment was performed under Proposal No. 2019A3811 at SPring-8 BL23SU. Work at Los Alamos National Laboratory was performed under the auspices of the U.S. Department of Energy, Office of Basic Energy Sciences, Division of Materials Science and Engineering under project "Quantum Fluctuations in Narrow-Band Systems."

DATA AVAILABILITY

The data supporting this study's findings are available within the article and can be made available in digital form upon reasonable request.

APPENDIX A: CROSS-SECTION CORRECTION

Table I lists the photoionization cross section used to account for the different photon energies when comparing the DFT + DMFT calculations with the experimental data. The values are calculated according to the expression $\sigma_i \times (1+\beta)/N$, where N is degeneracy of the shell, and σ and β are taken from Refs. [34–36]. For $h\nu = 800$ eV, the cross sections on a logarithmic scale are linearly interpolated between the values for $h\nu = 500$ and 1000 eV. Since cross sections for U $7p$ are not listed, we used the value for U $7s$, based on the empirical observation that photoionization cross-sections per electron are approximately equal for the

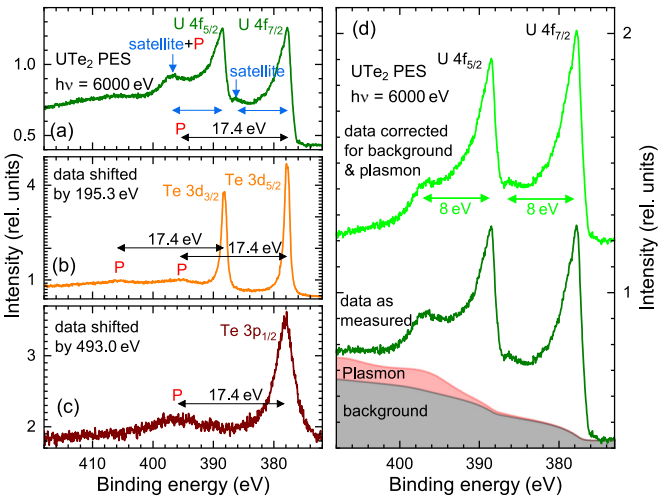

FIG. 5. UTe_2 HAXPES data: (a) U $4f$ core-level and (b), (c) shifted core-level spectra of Te $3d$ and Te $3p_{3/2}$, respectively. P marks plasmon scattering at 17.4 eV above the main absorption lines. (d) U $4f$ core level data of UTe_2 as measured (dark green) and after correction of the integral-type background and plasmon (light green) with satellites 8.2eV above the main emission lines. The filled areas below the original data represent the contribution from the integrated background (gray) and plasmons (red).

corresponding ns and np shells (where n is the principal quantum number).

APPENDIX B: BACKGROUND AND PLASMON CORRECTION OF CORE-LEVEL

Figure 5 shows U $4f$, Te $3d$, and Te $3p_{3/2}$ hard x-ray photoelectron spectroscopy data of UTe_2. The Te core levels that are not affected by configuration interaction effects are used to correct for some minor plasmon scattering at 17.4 eV higher binding energies from the main emission lines. The plasmons are present for all core levels. After subtracting the plasmon scattering from the U $4f$ core-level data, the remaining spectral weights, 8 eV above the U $4f$ core-level main emission lines, are due to satellites arising from configuration interaction.

APPENDIX C: IMPACT OF PARAMETERS, μ_{dc}, U_{ff}, AND J, ON DFT + DMFT CALCULATIONS

Figure 6(a) displays the μ_{dc} dependence of the corresponding DFT + DMFT VB spectra. The spectra are generated by multiplying the orbital-resolved DOS from the DFT + DMFT calculations with a Fermi function, convoluting with the experimental resolution, and correcting for the respective photoionization cross sections (see Table I). For comparison, all spectra, both experimental and calculated, are normalized to their integrated area within the displayed energy range. The spectra around $\mu_{dc} = 4.75$ eV resemble the data best.

The weights of the U $5f^n$ configurations in the ground state are sensitive to the choice of μ_{dc}, as shown in Fig. 6(b). For values of μ_{dc} greater than 4.75 eV (green bar), the $5f^3$

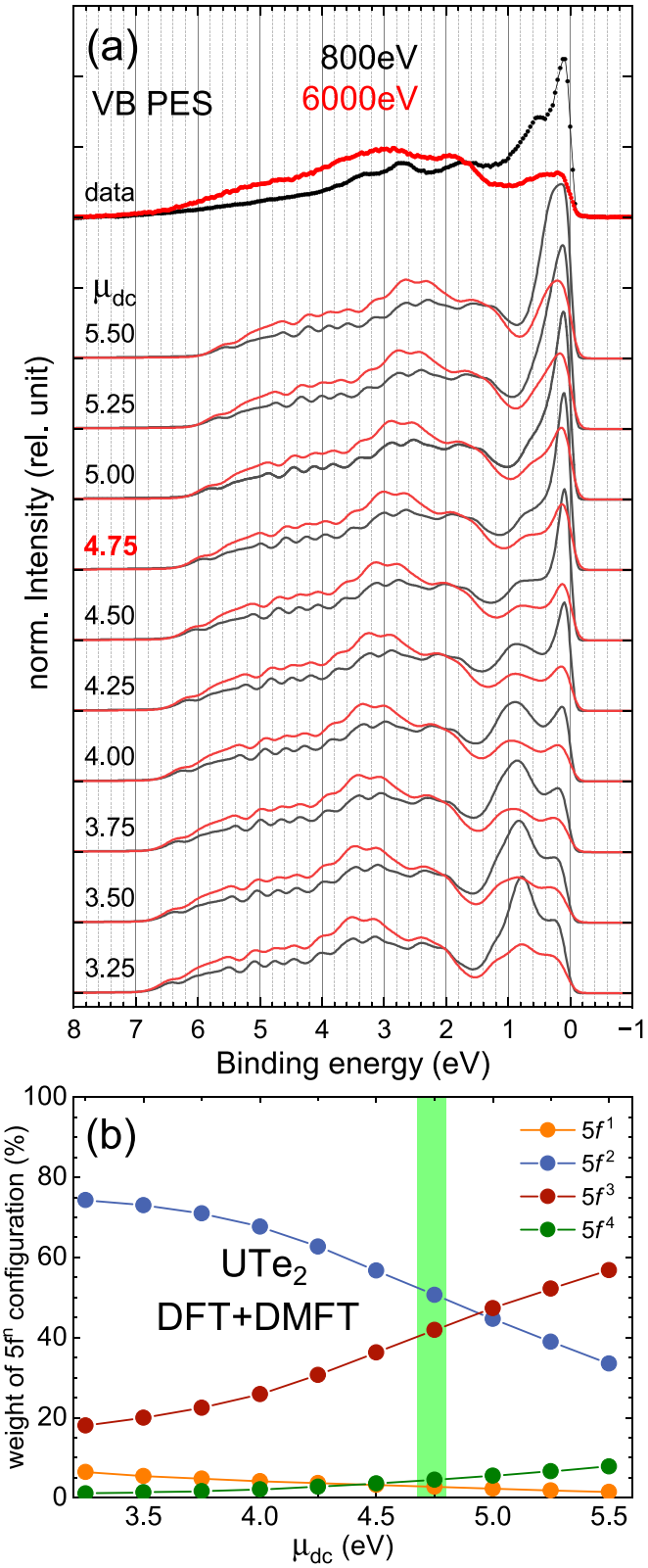

FIG. 6. (a) Experimental VB PES data measured with 800 and 6000 eV photon energies, compared to DFT + DMFT spectra calculated with $U_{ff} = 3$ eV and $J = 0.59$ eV for several μ_{dc} values. (b) Variation of the $5f^n$ weights as a function of μ_{dc} (in percent). The green bar indicates the optimum value of μ_{dc}.

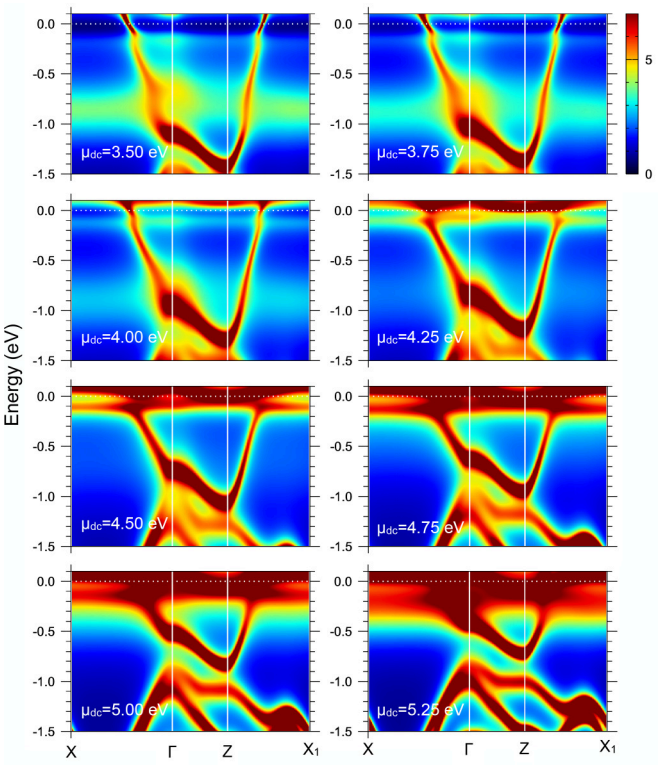

FIG. 7. Momentum-resolved spectral densities in the DFT + DMFT results for selected μ_{dc} values. The orbital-resolved densities for the optimal μ_{dc} and the experimental data are shown in Fig. 2.

configuration becomes dominant and also the $5f^4$ configuration gains weight. For smaller values of μ_{dc}, the $5f^2$ configuration becomes more prominent, eventually reaching a situation as in UGa_2 [33]. This behavior is expected as μ_{dc} renormalizes the U $5f$ orbital energy. In a simplified two-configuration picture, the $5f^2$ configuration lies lowest

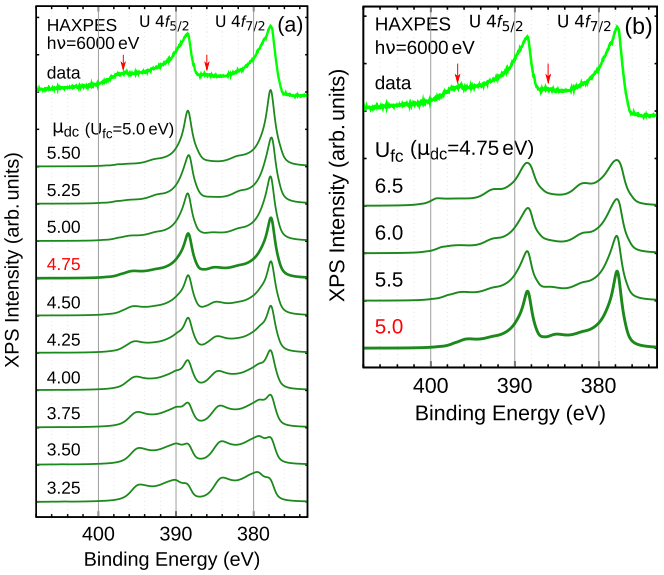

FIG. 8. (a) μ_{dc} dependence of DFT + DMFT AIM simulation of U $4f$ core-level spectra for fixed $U_{fc} = 5.0$ eV. (b) U_{fc} dependence for fixed $\mu_{dc} = 4.75$ eV.

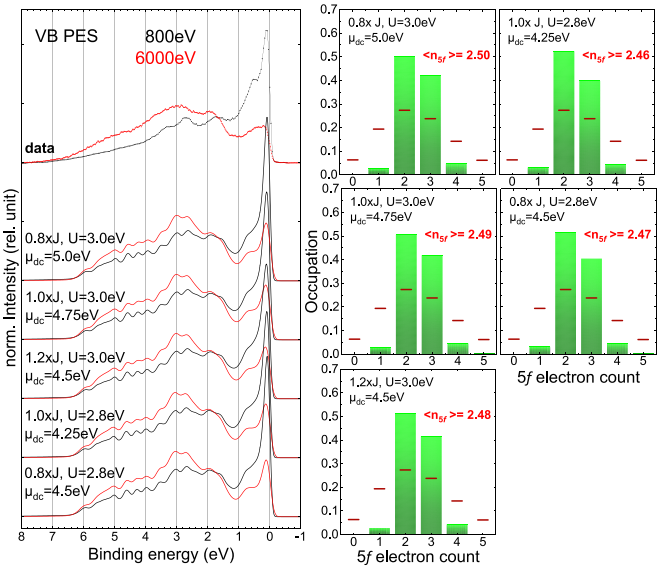

FIG. 9. Left: Experimental VB PES spectra measured with 800 and 6000 eV photon energies, compared to DFT + DMFT spectra for several sets of U_{ff} and J (with J scaled by 0.59 eV), using adjusted double-counting corrections μ_{dc} to match the experimental data. Right: Corresponding histograms of the $5f^n$ weights. The average $5f$ occupation $\langle n_f \rangle$ remains unchanged across all parameter sets.

in energy for small μ_{dc}, whereas for larger values, the $5f^3$ configuration becomes energetically favored, as the U $5f$ energy is given by $\varepsilon_{5f}^{\mathrm{DMFT}} = \varepsilon_{5f}^{\mathrm{DFT}} - \mu_{dc}$ (where $\varepsilon_{5f}^{\mathrm{DFT}}$ is the $5f$ energy in the DFT result). Coherent charge fluctuations can occur between the two configurations, mediated by intersite hybridization (itinerant, intermediate-valence case). When the energies of the two configurations are quasidegenerate, on-site fluctuations (local, mixed-valence case) between $5f^2$ and $5f^3$ may occur.

Figure 7 shows the evolution of the low-energy band structure in the DFT + DMFT results with varying the double-counting value μ_{dc}. Along the selected path in momentum space, there is a dispersive band extending from -0.5 eV at Γ to around -0.8 eV at the Z point, where its bottom in the adopted path is located. This dispersive band exhibits the hybridized character of the Te $5p$ and U $6d$ states. The U $5f$ states do not contribute in this energy range, as their spectral weight appears near the Fermi level [see panels (c)–(e) in Fig. 2]. As a result, the dispersive band shifts to higher energies relative to the U $5f$ states in a nearly monotonic fashion as μ_{dc} decreases (corresponding to a shallower $5f$ level). Thus, a direct comparison of the position of the dispersive band with the ARPES data in Fig. 2(a) provides a reasonable way to determine the μ_{dc} value.

The value $\mu_{dc} = 4.75$ eV yields good agreement in the dispersive feature with the experimental ARPES data. Furthermore, it produces a flat-band feature around -0.1 to -0.2 eV associated with U $5f$-dominated states. In addition to the dispersive band, the position and spectral intensities of the U $5f$ states are also sensitive to μ_{dc}, although their dependence exhibits a more complex behavior due to modulation of the correlation effects arising from changes in the U $5f$ valency. Therefore, both features show a deviation from the experimental data when μ_{dc} departs from this optimal value.

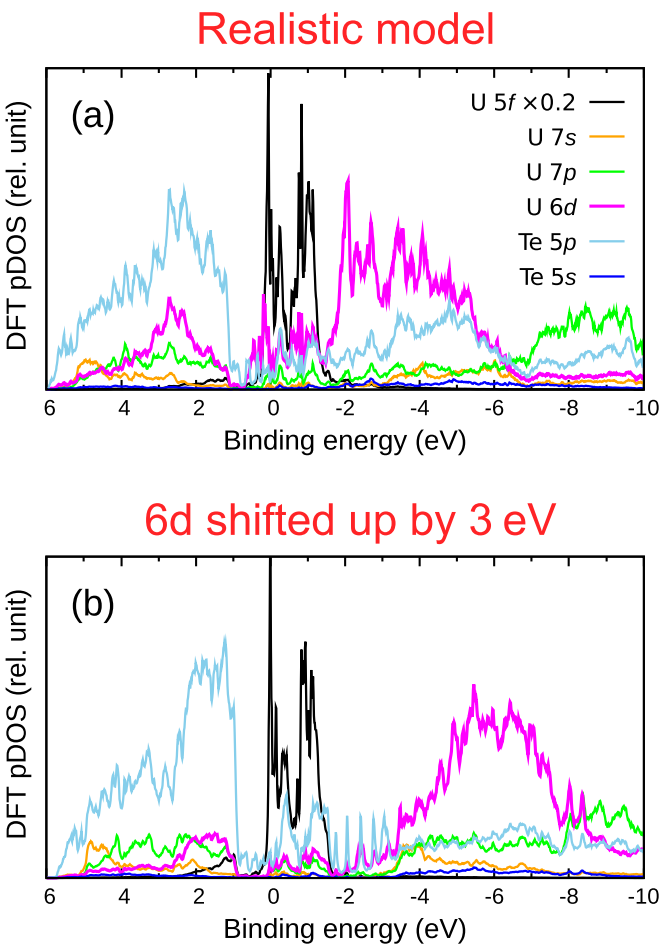

FIG. 10. DFT electronic structures used as input for the DMFT part in panel (a) for the *realistic* model, while in panel (b) for the *modified model*, in which the U 6*d* states are artificially eliminated from the top region of the VB.

Then, we proceed with the core-level spectra. Following Ref. [33], we neglect the orbital degrees of the core state; i.e., *s*-orbital symmetry of the core orbital is assumed in the simulation to make the computation feasible. In Ref. [33], the multiplet part of the core-valence interaction was found to be unimportant for the $4f$ core-level spectrum. Furthermore, because the U $4f_{5/2}$ and U $4f_{7/2}$ levels are sufficiently separated in energy (∼10 eV), interference between the two can safely be neglected. Thus, we simulated the total spectrum by accounting for the nominal degeneracy ratio of 6:8 in the $4f_{5/2,7/2}$ core states and by applying a 10 eV shift corresponding to the $4f$ spin-orbit splitting.

In Fig. 8, U $4f$ core-level HAXPES data of UTe_2 are compared to the DFT + DMFT AIM calculations for different μ_{dc} [in panel (a)] and core-hole potential U_{fc} values [in panel (b)]. The best agreement between experiment and theory is achieved for $\mu_{dc} = 4.75$ eV and $U_{fc} = 5.0$ eV. As μ_{dc} decreases below 4.25 eV, i.e., when enhancing the $5f^2$ configuration [see Fig. 6(b)], the satellite becomes at first more pronounced. With further decreasing μ_{dc}, the main emission line develops a substructure, reminiscent of the core-level spectra of strongly localized UPd_3. Also for values larger than the optimum μ_{dc}, the core level changes: The satellite 8 eV above the main

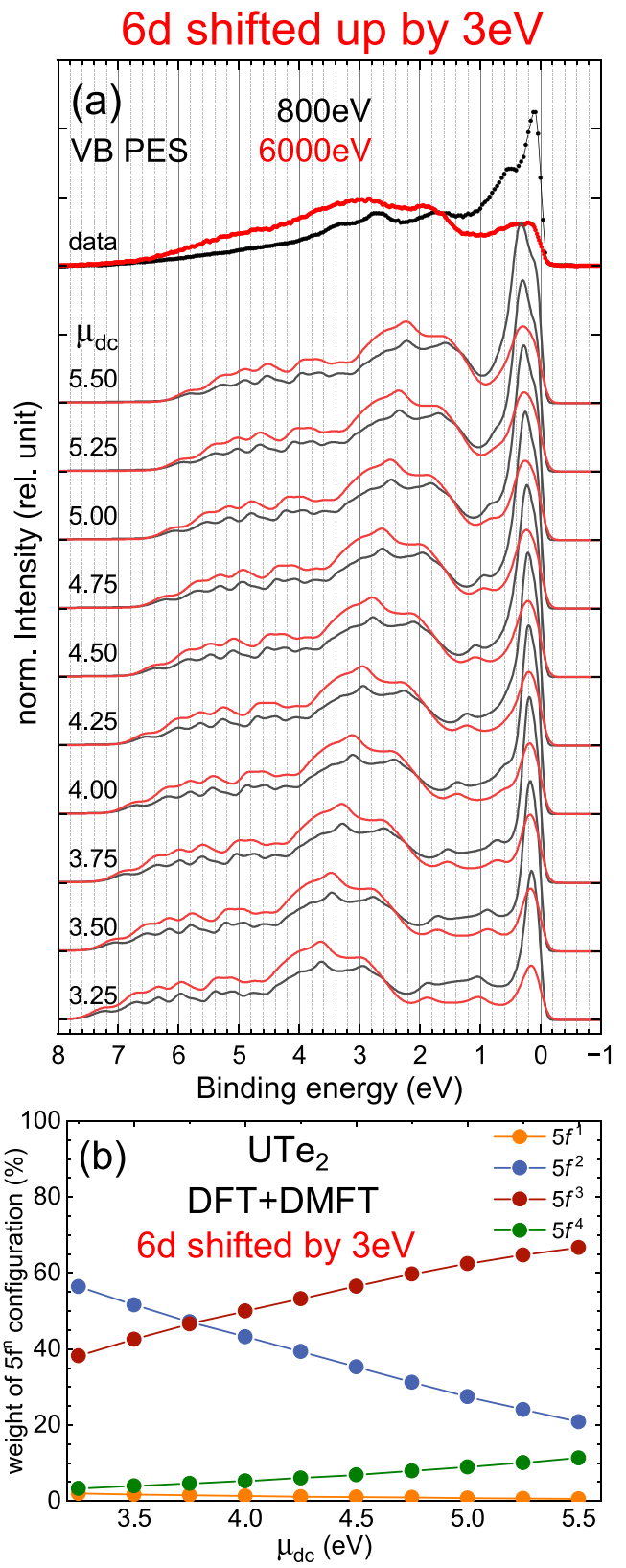

FIG. 11. (a) Experimental VB PES spectra measured with 800 and 6000 eV photon energies, compared to DFT + DMFT spectra calculated for the *modified model* with several μ_{dc} values. The stoichiometric electron count, identical to that of the realistic model, is properly implemented in the DMFT calculations. (b) Variation of the $5f^n$ weights (in percent) with μ_{dc} for the modified model.

emission line becomes weaker and another satellite, at lower binding energies, appears. The spectral shape also changes with U_{fc}. Also here, for large U_{fc}, the position of prime satellite changes and a third contribution appears.

Finally, we discuss the reliability of our estimation of the U valency with respect to the choice of the Hubbard U and Hund's J parameters. Figure 9 shows the DFT + DMFT-calculated VB spectra for several combinations of U_{ff} and J around the values adopted in the above analysis. The double-counting correction μ_{dc} must be adjusted to ensure agreement between data and calculation. Remarkably, for every parameter set that yields a good match with the data, the weights of the $5f^n$ configurations in the ground state are found to be nearly identical (see histogram plot in Fig. 9). In turn, the experimental spectra are only reproduced when the $5f^n$ weights are correctly captured.

APPENDIX D: LDA AND μ_{dc} DEPENDENCE OF DFT + DMFT SPECTRAL FUNCTIONS FOR 6*d*-REMOVED MODIFIED MODEL

Figures 10(a) and 10(b) show the LDA calculations used as input for the DFT + DMFT calculations. Panel (a) corresponds to the realistic model obtained for the experimental crystal structure of UTe_2. Practically, the valence spectral densities are computed from the tight-binding Hamiltonian derived from the LDA bands, as described in Sec. II. Panel (b), on the other hand, represents the *modified model* in which the participation of the U 6*d* states in the low-energy valence electronic structure is prohibited. This modified model is obtained by artificially shifting the 6*d* orbital energies in the LDA tight-binding Hamiltonian upward by 3 eV, which eliminates the U 6*d* contributions in the region near the top of the VB (in the -1 to 0 eV range). Apart from that, the noninteracting spectra do not differ significantly from the original realistic model [compare Figs. 6(a) and 6(b)]. However, once correlation effects are included within DMFT, this elimination leads to a large impact on the VB features.

The μ_{dc} dependence of the DFT + DMFT VB spectra in the modified model is displayed in Fig. 11(a). Also here the spectra are generated by multiplying the orbital-resolved DOS from the DFT + DMFT calculations with a Fermi function, convoluting with the experimental resolution, and correcting for the respective photoionization cross sections (see Table I). For comparison, all spectra, both experimental and calculated, are normalized to their integrated area within the displayed energy range. For the modified model, the VB data close to the Fermi energy cannot be reproduced for any set of parameters, confirming that it is unrealistic and that the U 6*d* states must be taken into account when modeling the electronic structure of UTe_2.

Figure 11(b) shows the evolution of the U $5f^n$ occupation as a function of μ_{dc} in the modified model. As the 6*d* states are not accessible, the $5f^3$ configuration becomes preferably occupied. This suggests that U ions favor the U^{3+} configuration in this case. Therefore, the experimental observation of a predominant U $5f^2$ configuration in VB-RIXS [20,26] strongly implies partial filling of the 6*d* states. This filling facilitates the U^{3+} character, so that the structure of UTe_2 does not have to accommodate two large Te^{2-} ions. Instead, one of the two Te ions can adopt the smaller configuration of Te^{-}.

[1] S. Ran, C. Eckberg, Q.-P. Ding, Y. Furukawa, T. Metz, S. R. Saha, I.-L. Liu, M. Zic, H. Kim, J. Paglione, and N. P. Butch, Nearly ferromagnetic spin-triplet superconductivity, Science **365**, 684 (2019).

[2] D. Aoki, A. Nakamura, F. Honda, D. Li, Y. Homma, Y. Shimizu, Y. J. Sato, G. Knebel, J.-P. Brison, A. Pourret, D. Braithwaite, G. Lapertot, Q. Niu, M. Vališka, H. Harima, and J. Flouquet, Unconventional superconductivity in heavy fermion UTe_2, J. Phys. Soc. Jpn. **88**, 043702 (2019).

[3] A. de Visser, UTe_2: A new spin-triplet pairing superconductor, JPSJ News Comments **16**, 08 (2019).

[4] H. Sakai, P. Opletal, Y. Tokiwa, E. Yamamoto, Y. Tokunaga, S. Kambe, and Y. Haga, Single crystal growth of superconducting UTe_2 by molten salt flux method, Phys. Rev. Mater. **6**, 073401 (2022).

[5] S. K. Lewin, C. E. Frank, S. Ran, J. Paglione, and N. P. Butch, A review of UTe_2 at high magnetic fields, Rep. Prog. Phys. **86**, 114501 (2023).

[6] Z. Wu, T. I. Weinberger, J. Chen, A. Cabala, D. V. Chichinadze, D. Shaffer, J. Pospíšil, J. Prokleška, T. Haidamak, G. Bastien, V. Sechovský, A. J. Hickey, M. J. Mancera-Ugarte, S. Benjamin, D. E. Graf, Y. Skourski, G. G. Lonzarich, M. Vališka, F. M. Grosche, and A. G. Eaton, Enhanced triplet superconductivity in next-generation ultra-clean UTe_2, Proc. Natl. Acad. Sci. USA **121**, e2403067121 (2024).

[7] G. Knebel, W. Knafo, A. Pourret, Q. Niu, M. Vališka, D. Braithwaite, G. Lapertot, M. Nardone, A. Zitouni, S. Mishra, I. Sheikin, G. Seyfarth, J.-P. Brison, D. Aoki, and J. Flouquet, Field-reentrant superconductivity close to a metamagnetic transition in the heavy-fermion superconductor UTe_2, J. Phys. Soc. Jpn. **88**, 063707 (2019).

[8] S. Ran, I.-L. Liu, Y. S. Eo, D. J. Campbell, P. M. Neves, W. T. Fuhrman, S. R. Saha, C. Eckberg, H. Kim, D. Graf, F. Balakirev, J. Singleton, J. Paglione, and N. P. Butch, Extreme magnetic field-boosted superconductivity, Nat. Phys. **15**, 1250 (2019).

[9] W. Knafo, T. Thebault, S. Raymond, P. Manuel, D. D. Khalyavin, F. Orlandi, E. Ressouche, K. Beauvois, G. Lapertot, K. Kaneko, D. Aoki, D. Braithwaite, and G. Knebel, Incommensurate antiferromagnetism in UTe_2 under pressure, Phys. Rev. X **15**, 021075 (2025).

[10] S. M. Thomas, F. B. Santos, M. H. Christensen, T. Asaba, F. Ronning, J. D. Thompson, E. D. Bauer, R. M. Fernandes, G. Fabbris, and P. F. S. Rosa, Evidence for a pressure-induced antiferromagnetic quantum critical point in intermediate-valence UTe_2, Sci. Adv. **6**, eabc8709 (2020).

[11] S. Ran, H. Kim, I.-L. Liu, S. R. Saha, I. Hayes, T. Metz, Y. S. Eo, J. Paglione, and N. P. Butch, Enhancement and reentrance of spin triplet superconductivity in UTe_2 under pressure, Phys. Rev. B **101**, 140503(R) (2020).

[12] L. Q. Huston, D. Y. Popov, A. Weiland, M. M. Bordelon, P. F. S. Rosa, R. L. Rowland, B. L. Scott, G. Shen, C. Park, E. K. Moss,

S. M. Thomas, J. D. Thompson, B. T. Sturtevant, and E. D. Bauer, Metastable phase of UTe_2 formed under high pressure above 5 GPa, Phys. Rev. Mater. **6**, 114801 (2022).

[13] F. Honda, S. Kobayashi, N. Kawamura, S. I. Kawaguchi, T. Koizumi, Y. J. Sato, Y. Homma, N. Ishimatsu, J. Gouchi, Y. Uwatoko, H. Harima, J. Flouquet, and D. Aoki, Pressure-induced structural phase transition and new superconducting phase in UTe_2, J. Phys. Soc. Jpn. **92**, 044702 (2023).

[14] Y. Deng, E. Lee-Wong, C. M. Moir, R. S. Kumar, N. Swedan, C. Park, D. Y. Popov, Y. Xiao, P. Chow, R. E. Baumbach, R. J. Hemley, P. S. Riseborough, and M. B. Maple, Structural transition and uranium valence change in UTe_2 at high pressure revealed by x-ray diffraction and spectroscopy, Phys. Rev. B **110**, 075140 (2024).

[15] F. Wilhelm, J.-P. Sanchez, D. Braithwaite, G. Knebel, G. Lapertot, and A. Rogalev, Investigating the electronic states of UTe_2 using x-ray spectroscopy, Commun. Phys. **6**, 96 (2023).

[16] J. Allen, J.-S. Kang, Y. Lassailly, M. Maple, M. Torikachvili, W. Ellis, B. Pate, and I. Lindau, Electron spectroscopy study of the heavy fermion compound URu_2Si_2, Solid State Commun. **61**, 183 (1987).

[17] A. Kotani and T. Yamazaki, Systematic analysis of core photoemission spectra for actinide di-oxides and rare-earth sesqui-oxides, Prog. Theor. Phys. Suppl. **108**, 117 (1992),.

[18] F. de Groot and A. Kotani, *Core Level Spectrocopy of Solis*, edited by D.D. Sarma, G. Kotliar, and Y. Tokura, Advances in Condensed Matter Science Vol. 6 (CRC Press, Boca Raton, 2008).

[19] S.-I. Fujimori, I. Kawasaki, Y. Takeda, H. Yamagami, A. Nakamura, Y. Homma, and D. Aoki, Electronic structure of UTe_2 studied by photoelectron spectroscopy, J. Phys. Soc. Jpn. **88**, 103701 (2019).

[20] L. Miao, S. Liu, Y. Xu, E. C. Kotta, C.-J. Kang, S. Ran, J. Paglione, G. Kotliar, N. P. Butch, J. D. Denlinger, and L. A. Wray, Low energy band structure and symmetries of UTe_2 from angle-resolved photoemission spectroscopy, Phys. Rev. Lett. **124**, 076401 (2020).

[21] S.-I. Fujimori, I. Kawasaki, Y. Takeda, H. Yamagami, A. Nakamura, Y. Homma, and D. Aoki, Core-level photoelectron spectroscopy study of UTe_2, J. Phys. Soc. Jpn. **90**, 015002 (2021).

[22] A. B. Shick, S.-I. Fujimori, and W. E. Pickett, UTe_2: A nearly insulating half-filled $j = \frac{5}{2} 5f^3$ heavy-fermion metal, Phys. Rev. B **103**, 125136 (2021).

[23] D. Aoki, H. Sakai, P. Opletal, Y. Tokiwa, J. Ishizuka, Y. Yanase, H. Harima, A. Nakamura, D. Li, Y. Homma, Y. Shimizu, G. Knebel, J. Flouquet, and Y. Haga, First observation of the de Haas–van Alphen effect and Fermi surfaces in the unconventional superconductor UTe_2, J. Phys. Soc. Jpn. **91**, 083704 (2022).

[24] S. Liu, Y. Xu, E. C. Kotta, L. Miao, S. Ran, J. Paglione, N. P. Butch, J. D. Denlinger, Y.-D. Chuang, and L. A. Wray, Identifying f-electron symmetries of UTe_2 with O-edge resonant inelastic x-ray scattering, Phys. Rev. B **106**, L241111 (2022).

[25] A. Marino, M. Sundermann, D. S. Christovam, A. Amorese, C.-F. Chang, P. Dolmantas, A. H. Said, H. Gretarsson, B. Keimer, M. W. Haverkort, A. V. Andreev, L. Havela, P. Thalmeier, L. H. Tjeng, and A. Severing, Singlet magnetism in intermetallic UGa_2 unveiled by inelastic x-ray scattering, Phys. Rev. B **108**, 045142 (2023).

[26] D. S. Christovam, M. Sundermann, A. Marino, D. Takegami, J. Falke, P. Dolmantas, M. Harder, H. Gretarsson, B. Keimer, A. Gloskovskii, M. W. Haverkort, I. Elfimov, G. Zwicknagl, A. V. Andreev, L. Havela, M. M. Bordelon, E. D. Bauer, P. F. S. Rosa, A. Severing, and L. H. Tjeng, Stabilization of U $5f^2$ configuration in UTe_2 through U $6d$ dimers in the presence of Te_2 chains, Phys. Rev. Res. **6**, 033299 (2024).

[27] O. Gunnarsson and K. Schönhammer, Electron spectroscopies for Ce compounds in the impurity model, Phys. Rev. B **28**, 4315 (1983).

[28] O. Gunnarsson, D. D. Sarma, F. U. Hillebrecht, and K. Schönhammer, Electronic structure of the light actinide oxides from electron spectroscopy (invited), J. Appl. Phys. **63**, 3676 (1988).

[29] A. Kotani, T. Jo, and J. Parlebas, Many-body effects in core-level spectroscopy of rare-earth compounds, Adv. Phys. **37**, 37 (1988).

[30] A. Kotani, Theory of core-level spectroscopy in f and d electron systems, J. Electron Spectrosc. Relat. Phenom. **100**, 75 (1999).

[31] S.-I. Fujimori, T. Ohkochi, I. Kawasaki, A. Yasui, Y. Takeda, T. Okane, Y. Saitoh, A. Fujimori, H. Yamagami, Y. Haga, E. Yamamoto, Y. Tokiwa, S. Ikeda, T. Sugai, H. Ohkuni, N. Kimura, and Y. Onuki, Electronic structure of heavy fermion uranium compounds studied by core-level photoelectron spectroscopy, J. Phys. Soc. Jpn. **81**, 014703 (2012).

[32] S.-I. Fujimori, Y. Takeda, T. Okane, Y. Saitoh, A. Fujimori, H. Yamagami, Y. Haga, E. Yamamoto, and Y. Ōnuki, Electronic structures of uranium compounds studied by soft x-ray photoelectron spectroscopy, J. Phys. Soc. Jpn. **85**, 062001 (2016).

[33] A. Marino, D. S. Christovam, D. Takegami, J. Falke, M. M. F. Carvalho, T. Okauchi, C.-F. Chang, S. G. Altendorf, A. Amorese, M. Sundermann, A. Gloskovskii, H. Gretarsson, B. Keimer, A. V. Andreev, L. Havela, A. Leithe-Jasper, A. Severing, J. Kuneš, L. H. Tjeng, and A. Hariki, Quantifying the U $5f$ covalence and degree of localization in U intermetallics, Phys. Rev. Res. **6**, 033068 (2024).

[34] M. Trzhaskovskaya, V. Needov, and V. Yarzhemsky, Photoelectron angular distribution parameters for elements Z = 1 to Z = 54 in the photoelectron energy range 100–5000 eV, At. Data Nucl. Data Tables **77**, 97 (2001).

[35] M. Trzhaskovskaya, V. Needov, and V. Yarzhemsky, Photoelectron angular distribution parameters for elements Z = 55 to Z = 100 in the photoelectron energy range 100–5000 eV, At. Data Nucl. Data Tables **82**, 257 (2002).

[36] M. Trzhaskovskaya and V. Yarzhemsky, Dirac–Fock photoionization parameters for HAXPES applications, At. Data Nucl. Data Tables **119**, 99 (2018).

[37] Y. Saitoh, Y. Fukuda, Y. Takeda, H. Yamagami, S. Takahashi, Y. Asano, T. Hara, K. Shirasawa, M. Takeuchi, T. Tanaka, and H. Kitamura, Performance upgrade in the JAEA actinide science beamline BL23SU at spring-8 with a new twin-helical undulator, J. Synchrotron Radiat. **19**, 388 (2012).

[38] C. Schlueter, A. Gloskovskii, K. Ederer, I. Schostak, S. Piec, I. Sarkar, Y. Matveyev, P. Lömker, M. Sing, R. Claessen, C. Wiemann, C. M. Schneider, K. Medjanik, G. Schönhense, P. Amann, A. Nilsson, and W. Drube, The new dedicated HAXPES beamline P22 at PETRA III, AIP Conf. Proc. **2054**, 040010 (2019).

[39] V. Hutanu, H. Deng, S. Ran, W. T. Fuhrman, H. Thoma, and N. P. Butch, Low-temperature crystal structure of the unconventional spin-triplet superconductor UTe_2 from single-crystal neutron diffraction, Acta Crystallogr. Sect. B **76**, 137 (2020).

[40] P. Blaha, K. Schwarz, G. Madsen, D. Kvasnicka, and J. Luitz, *WIEN2k, An Augmented Plane Wave + Local Orbitals Program for Calculating Crystal Properties* (Karlheinz Schwarz, Technische Universitat Wien, Austria, 2001).

[41] J. Kuneš, R. Arita, P. Wissgott, A. Toschi, H. Ikeda, and K. Held, Wien2wannier: From linearized augmented plane waves to maximally localized Wannier functions, Comput. Phys. Commun. **181**, 1888 (2010).

[42] A. A. Mostofi, J. R. Yates, G. Pizzi, Y.-S. Lee, I. Souza, D. Vanderbilt, and N. Marzari, An updated version of wannier90: A tool for obtaining maximally-localised Wannier functions, Comput. Phys. Commun. **185**, 2309 (2014).

[43] A. Georges, G. Kotliar, W. Krauth, and M. J. Rozenberg, Dynamical mean-field theory of strongly correlated fermion systems and the limit of infinite dimensions, Rev. Mod. Phys. **68**, 13 (1996).

[44] G. Kotliar, S. Y. Savrasov, K. Haule, V. S. Oudovenko, O. Parcollet, and C. A. Marianetti, Electronic structure calculations with dynamical mean-field theory, Rev. Mod. Phys. **78**, 865 (2006).

[45] P. Werner, A. Comanac, L. de'Medici, M. Troyer, and A. J. Millis, Continuous-time solver for quantum impurity models, Phys. Rev. Lett. **97**, 076405 (2006).

[46] E. Gull, A. J. Millis, A. I. Lichtenstein, A. N. Rubtsov, M. Troyer, and P. Werner, Continuous-time Monte Carlo methods for quantum impurity models, Rev. Mod. Phys. **83**, 349 (2011).

[47] L. Boehnke, H. Hafermann, M. Ferrero, F. Lechermann, and O. Parcollet, Orthogonal polynomial representation of imaginary-time Green's functions, Phys. Rev. B **84**, 075145 (2011).

[48] H. Hafermann, K. R. Patton, and P. Werner, Improved estimators for the self-energy and vertex function in hybridization-expansion continuous-time quantum Monte Carlo simulations, Phys. Rev. B **85**, 205106 (2012).

[49] M. Jarrell and J. Gubernatis, Bayesian inference and the analytic continuation of imaginary-time quantum Monte Carlo data, Phys. Rep. **269**, 133 (1996).

[50] M. Karolak, G. Ulm, T. Wehling, V. Mazurenko, A. Poteryaev, and A. Lichtenstein, Double counting in LDA+DMFT—The example of NiO, J. Electron Spectrosc. Relat. Phenom. **181**, 11 (2010).

[51] K. Haule, Exact double counting in combining the dynamical mean-field theory and the density functional theory, Phys. Rev. Lett. **115**, 196403 (2015).

[52] A. Hariki, T. Uozumi, and J. Kuneš, LDA+DMFT approach to core-level spectroscopy: Application to $3d$ transition metal compounds, Phys. Rev. B **96**, 045111 (2017).

[53] S.-I. Fujimori, M. Kobata, Y. Takeda, T. Okane, Y. Saitoh, A. Fujimori, H. Yamagami, Y. Haga, E. Yamamoto, and Y. Ōnuki, Manifestation of electron correlation effect in $5f$ states of uranium compounds revealed by $4d - 5f$ resonant photoelectron spectroscopy, Phys. Rev. B **99**, 035109 (2019).

[54] A. Bosch, Photoelectron spectroscopy, new angle-resolved spectrometer and study of dilute alloys, Ph.D. thesis, University of Groningen, 1982.

[55] E. R. Ylvisaker, J. Kuneš, A. K. McMahan, and W. E. Pickett, Charge fluctuations and the valence transition in Yb under pressure, Phys. Rev. Lett. **102**, 246401 (2009).

[56] Y. Xu, Y. Sheng, and Y.-F. Yang, Quasi-two-dimensional Fermi surfaces and unitary spin-triplet pairing in the heavy fermion superconductor UTe_2, Phys. Rev. Lett. **123**, 217002 (2019).

[57] H. C. Choi, S. H. Lee, and B.-J. Yang, Correlated normal state fermiology and topological superconductivity in UTe_2, Commun. Phys. **7**, 273 (2024).

[58] B. Kang, Y. Lee, L. Ke, H. Kim, M.-H. Kim, and C. H. Park, Dual nature of magnetism driven by momentum dependent f-d Kondo hybridization, Commun. Phys. **7**, 186 (2024).